A Modular and High-Precision Motion Control System With an Integrated Motor

Farhad Aghili, *Senior Member, IEEE*, John M. Hollerbach, *Fellow, IEEE*, and Martin Buehler, *Member, IEEE*

***Abstract*—This paper describes the design and control of an integrated direct-drive joint suitable for applications that require a high-precision motion control system. The joint integrates a direct-drive synchronous motor with axial air gap, a torque sensor, and a high-resolution position sensor. The key design aspects of the integrated joint, like the motor's armature, cooling system, motor housing, bearing arrangement, sensors, and power electronics are detailed. We also present a number of advanced implementations in motor torque control, optimal joint torque sensory feedback, and motion control using positive joint torque feedback. Experimental results illustrate an outstanding performance regarding thermal response, torque ripple, reference trajectory tracking, torque disturbance rejection, and joint stiffness.**

***Index Terms*—Actuator, brushless motor, direct-drive motor, integrated mechatronics, mechatronics system, modular controller, modular joint, motion control system, robot joint, robust control.**

I. Introduction

HIGH-PERFORMANCE motion control systems are key components in the modern robotics and automation industries. In particular, industrial robots for laser cutting, arc welding, fixture-less assembly, flexible manufacturing, indexing, or computer numerical control (CNC) machine tools require precise and high-bandwidth tracking accuracy as well as good disturbance rejection properties. Conventional electric motors with their high speed and low torque are not ideal for these tasks, since they require gears that degrade performance due to backlash, stiction, friction, and compliance. Internal friction in gears introduces motor torque losses of 10%–50%. Moreover, a gear ratio n multiplies the motor's rotor inertia seen by the load by n^2 that further reduces the maneuverability and bandwidth of geared robots [1].

These disadvantages are avoided or reduced with direct-drive actuators, which can produce the torque–speed characteristics required in many high-performance motion control tasks without additional gearing [1], [2]. The main advantages claimed for direct-drive robots are high accuracy and speed, light weight, high stiffness, and mechanical design simplicity. However, direct-drive systems are more sensitive to the actuator's torque ripple, and they also suffer from lower continuous torque compared to geared motors. Moreover, they are sensitive to load torques due to the lack of the attenuation effect of a gearbox. In light of these shortcomings, we have pursued a multiobjective agenda toward improving direct-drive joint performance. For instance, torque-to-mass ratio can be improved by reducing the motor's thermal resistance through special design of the motor's armature [3]–[5] and by minimizing power losses through optimal commutation [6]. The motor torque ripple can be reduced by improving motor design such as skewing and fractional slot pitch windings [7], and by implementing a proper torque control. The sensitivity of the direct-drive joint to load torque can be suppressed via positive joint torque feedback [8], [9] if it is possible to integrate a suitable torque sensor [10].

Axial air gap synchronous motors were identified to be superior for direct-drive actuation [3], [4], and several prototypes of such a motor, the "McGill/MIT" [3], [4] motor, in single axial air gap configurations have been constructed. The key design feature—a "pancake" shape armature with *water cooling*—increases the allowable continuous current, and therefore, the torque-to-mass ratio. This paper describes the design and control system of the fourth iteration of the McGill/MIT motor, and the components of the complete direct-drive system and the experimental tools necessary for its calibration, control, and performance test (Fig. 6). A number of advanced implementations on this motor have been presented in the past that address the minimization of torque ripple [6] and motion control using positive joint torque feedback [9].

Originally, the motor and its control system were specifically designed for the shoulder joints of a high-speed direct-drive robotic system. However, other mechatronics applications requiring high-speed tracking and positioning systems can benefit from the proposed motion control system. The joint sensory feedback makes the system modular and inherently robust with respect to uncertain or varying loads. Moreover, the mechanical design allows the presence of strong overhung force and bending moments in the joint. Thus, the integrated joint and its controller are particularly useful in applications such as robotic manipulators, CNC machine tools, and radar-tracking antenna. In these examples, the inertial/graviational forces of the links, cutting force, and wind force are the mechanical loads that constitute either a varying or uncertain torsional moment exerting to the motion control system and strong nontorsional force components applying to the motor's housing, bearing, and torque sensor.

This paper is organized as follows. Section II describes the design of the direct-drive joint along with the system components and the related experimental hardware that will be used subsequently. The main objective of the section encompasses the armature design, while engineering issues in the design of

Manuscript received March 1, 2006; revised December 15, 2006. Recommended by Guest Editors H.-P. Huang and F.-T. Cheng.

F. Aghili is with the Canadian Space Agency, Saint-Hubert, QC J3Y 8Y9, Canada, and also with the Mechanical and Industrial Engineering Department, Concordia University, Montreal, QC H3G 1M8, Canada (e-mail: farhad.aghili@space.gc.ca).

J. M. Hollerbach is with the School of Computing, University of Utah, Salt Lake City, UT 84112 USA (e-mail: jmh@cs.utah.edu).

M. Buehler is with Robotics, Boston Dynamics, Cambridge, MA 02139 USA (e-mail: buehler@bostondynamics.com).

Digital Object Identifier 10.1109/TMECH.2007.897273

the motor, specifically the motor's housing and bearing configuration will be also discussed. The thermal aspect of the motor is also characterized experimentally. The motor is equipped with a specifically designed torque sensor that is described in Section II-E. The mechanical structure and geometry of this sensor is carefully designed to be suitable for joint torque measurement and its prominent mechanical features are proven experimentally. It follows a brief description of a hydraulic dynamometer in Section III that is used to calibrate the motor and to test the dynamic behavior of the motor and its entire control system. The remainder of this paper presents a systematic control design. The primary control design goal is high fidelity driving torque while maintaining minimum copper losses (to contribute further to maximize the motor's continuous torque) and maximize peak torque that is addressed in Section IV-B. Section IV-C presents a motion control with positive joint torque feedback where the actuator can provide precise and instantaneous driving torque. In this case, the dynamics of the robot with positive joint torque feedback is determined completely by the motion of the motor rotors in the Cartesian space that is not detectable by the torque sensors. Finally, the assumption of an ideal actuator in the analysis and design of joint torque feedback is relaxed in Section IV-D where the actuator dynamics is considered. The optimal feedback minimizes the load perturbation and makes the actual system close to the nominal rotor dynamics of the motor.

II. Motor Design

A. General Description

The main shortcoming of direct-drive motors is their low continuous torque compared to geared motors. This problem can be solved partially by special robot and/or motor design. The general trend in direct-drive robot design is to arrange the motors in configurations that minimize the gravitational torques [3]. Although the torque-to-mass ratio of the actuators plays a key role for high-performance direct-drive robots, there exists little research targeting the improvement of the technology of direct-drive actuators *per se* [3]–[5]. Variable-reluctance and permanent-magnet synchronous direct-drive motors have been widely used. However, the torque-to-mass ratio even in today's commercial direct-drive motors is still not sufficient for robotic applications. Wound-field synchronous motors were identified to be superior for direct-drive actuation [3], [4]. Accordingly, several prototypes of such a motor, the "McGill/MIT" [3] motor, in single axial air gap configurations have been constructed. In these motors, water cooling is used to increase the allowable continuous current and further enhance the overall torque-to-mass ratio. The motor prototype presented herein is the fourth iteration of this type of motor.

Fig. 1 illustrates the design of the motor whose design goal is to solve the main problems with direct-drive electric motors: large size and weight of theses motors relative to their torque and torque ripple production [3], [11]. The motor is a three-phase synchronous device with axial air gap that optimizes torque-to-mass ratio [3]. The axial air gap, however, introduces an extensive attractive force between the armatures that create a reaction

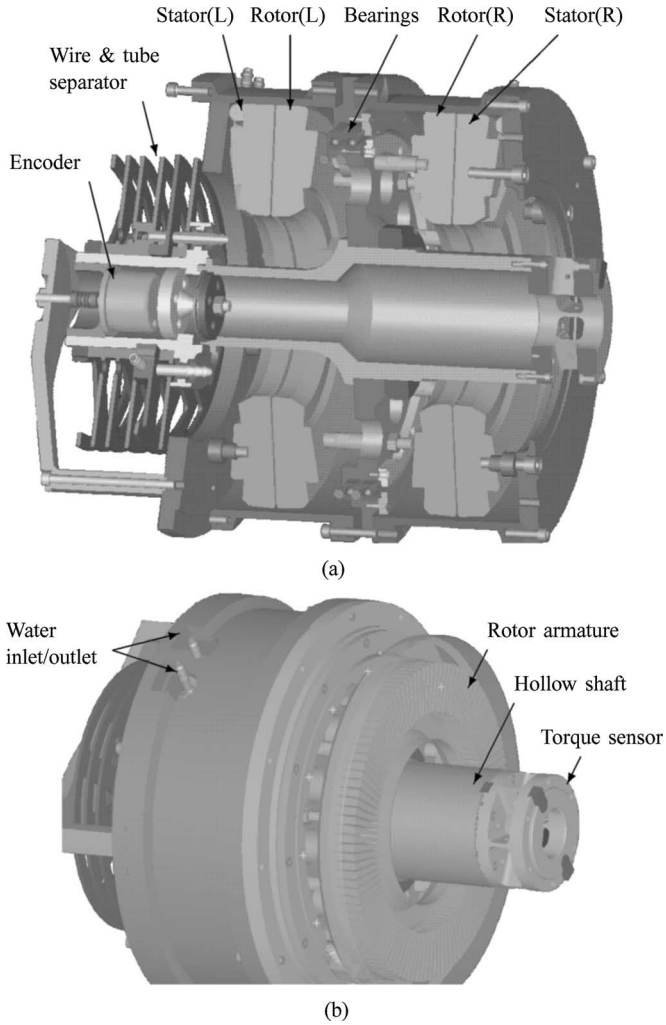

Fig. 1. Integrated design of the actuator and the sensors. (a) Cross-sectional view of the motor. (b) Right stator cap is removed.

force on the motor's bearings. To balance the axial force, we integrate two motors back-to-back such that the axial forces are taken by the motor's aluminum housing, as shown in Fig. 1(a). The armatures in the middle (rotors) are the rotating parts that are mounted in the motor's shaft while the two other armatures (stators) are mounted in the motor's housing. The bearing arrangement is carefully designed to minimize friction and weight as well as to maximize stiffness. Water cooling of the armatures is another feature of the design that improves the capability of the system to remove heat. Position sensing is required to perform both electronic commutation and motion control. An optical encoder (Teledyne Gurley 8321-4500-CBQA-NB) is mounted to the motor shaft while the encoder shaft is fixed to the motor's housing by a small bellow-type coupling (see Fig. 1). The resolution of the encoder is multiplied 80 times by an interpolator for 0.001° final resolution.

B. Armature

1) Core Design: Most electric motors deliver their maximum power at high velocity. The number of poles in motors plays the role of the gear ratio in gears that typically reduces

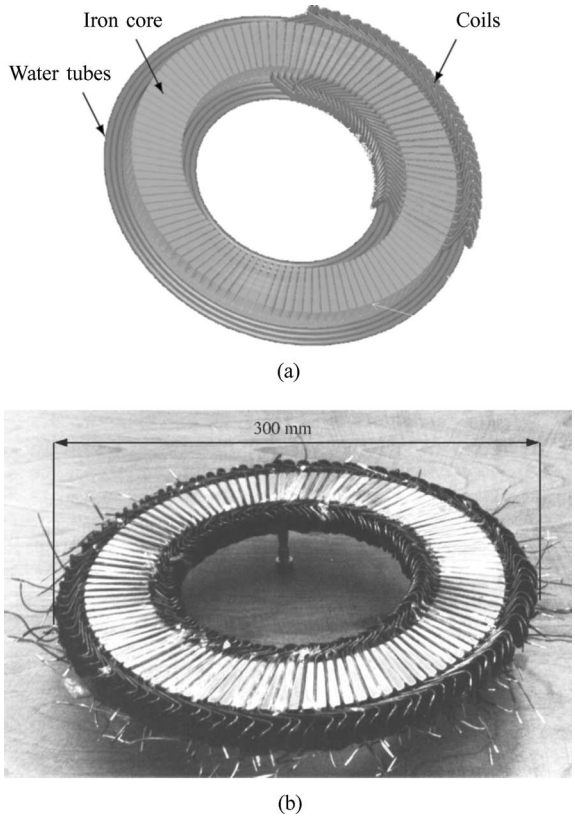

Fig. 2. Armature with 108 skewed slots. (a) Armature design. (b) Coils assembled in the core.

velocity and increases torque. However, increasing the number of poles has several practical limitations. Multipole motors require complex designs with many slots and windings, which increases the cost. In addition, they require high-frequency control signals that can be challenging for electronic commutators [6], [12]. Therefore, the number of poles and slots should be determined by a tradeoff between manufacturing capability and controllability. Fig. 2(b) shows the armature prototype with three phases wound over six slots per pole to create 18 poles. The resulting 108 slots are skewed by a full slot pitch to minimize torque ripple. The armature core is machined out of a ring rolled from a sheet of standard transformer iron that minimizes core losses. Glue treatment is performed between sheets during the lamination to solidify the laminated core. Although core losses tend to increase with sheet thickness, very thin sheets are not efficient because of the high occupancy ratio of the isolation layer and of the glue. We chose 0.5-mm-thick strip to make the laminated core with inside and outside diameters of 180 and 260 mm. In order to maximize packing factor, the armature coil is made of square wire—28 gauge.

2) Thermodynamics and Maximum Continuous Torque: The maximum motor torque is determined by the maximum allowable current subject to magnetic saturation. Magnetic saturation is a material-dependent property while the maximum winding current depends on thermal characteristics of a motor. Since magnetic saturation occurs almost instantaneously and the thermal time constant is relatively large, the magnetic saturation and thermal saturation dictate the motor's instantaneous and continuous torque capability, respectively. Since, typically, the continuous torque is the lower limit, it is maximized in our motor prototype. In the case of wound-field motors, the maximum attainable continuous torque $\tau_{\rm cont}$ is proportional to the square of the maximum admissible current i^2, which is, in turn, proportional to the maximum power loss $P_{\max}$. Therefore, we can say the maximum continuous torque is proportional to the maximum heat that the motor can dissipate before reaching the maximum temperature, i.e., $\tau_{\rm cont} \propto P_{\max}$.

The motor thermodynamics is a distributed system that can be divided into two copper winding and iron core subsystems. Since copper, and to some extent, iron have good thermal conductivity, the windings and core can be considered as a lumped system with *heat capacity* c. Also, assume that $R_{\rm th}, T$, and T_o represent the thermal resistance of the armature, the armature temperature, and the ambient temperature, respectively. Then, the principal of conservation of energy leads to the differential equation of the temperature

$$c\dot{T} = -\frac{T - T_o}{R_{\rm th}} + P(t).$$

The step response of the system with respect to maximum power loss is

$$T_\Delta = R_{\rm th} P_{\max}(1 - e^{-t/\mu}) \tag{1}$$

where $T_\Delta = T - T_o$ is the maximum temperature rise and $\mu = R_{\rm th}c$ is the time constant of the thermal system. At steady state, ΔT is equal to the maximum allowable power losses times the thermal resistance. Therefore, it can be concluded that

$$\tau_{\rm cont} \propto \frac{1}{R_{\rm th}} \tag{2}$$

which implies that the maximum torque is inversely proportional to the capability of the motor to remove heat, requiring a low thermal resistance.

Most motors dissipate heat by convection and radiation. This is not very effective. Much better cooling can be achieved by water circulation, which increases the torque-to-mass ratio. It is imperative to bring the water circulation in proximity to the heat-producing copper windings. Fig. 2(a) shows the design of the armature where several copper tubes are placed close to the windings to provide adequate cooling. The armatures were potted in thermally conductive epoxy (Emerson and Cumming Stycast 2850FT) to improve the thermal conductivity between the copper windings and the cooling tubes. To monitor the thermodynamic behavior of the motor, six thermocouples (Omega JMTSS-02OU-6) are placed in the vicinity of each winding phase of the rotor and stator.

3) Thermal Test: The preliminary test indicated that the rotor and stator armatures have identical thermal responses; hence, only the rotor armature was studied in further thermal tests. The thermal step responses of the motor armature to different currents are shown in Fig. 3. The solid and dashed curves correspond to the system response with and without water circulation. The exponential temperature curves resemble the response of a first order system. It is quite clear that the system time constant

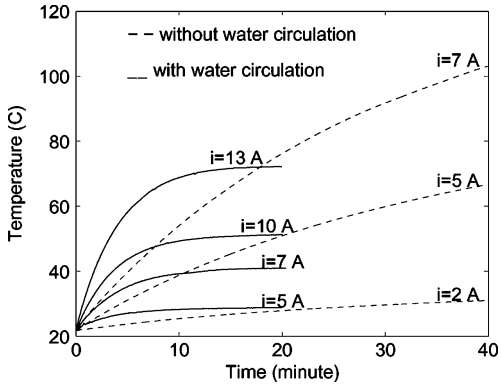

Fig. 3. Thermal step responses of the armature.

decreases considerably by water circulation and so does the asymptotic temperature. The slope of the lines approximates the thermal resistances of the windings to the ambient air with and without water cooling are 0.42 and 0.07 $^{\circ}\mathrm{C/W}$, respectively. Thus, by virtue of (2), one can conclude that the water cooling improves the continuous torque capability by a factor of 6.

Another key feature of a direct-drive joint is limited joint rotation, and hence, limited motor rotation. The maximum motor excursion can be expected to be limited to 360°. Since the motor is not required to rotate more than 360°, the connections for water cooling across the air gap as well as electrical connection to the rotor are made without slip rings. Fig. 1 illustrates the cable routing and the tube routing are separated by an array of aluminum discs.

C. Motor Housing

The motor housing contributes nothing to torque production, but can significantly decrease the motor's torque-to-mass ratio. Therefore, it is vital to minimize its weight while maintaining its strength. The housing elasticity permits the magnetic forces to reduce the air gap, which, in turn, increases the magnetic forces. As a consequence, the air gap can collapse. The subsequent analysis will determine the minimum stiffness for a *stable air gap*.

Let us assume that δ_{gap} and f_{ax} are, respectively, the air gap distance in the absence of any elastic deflection and the axial force on the armature. Also assume that the elasticity of the housing is represented by its axial stiffness k_{hous}. Then, the flexible housing may buckle [11] if

$$k_{\mathrm{hous}} \geq k_c = \frac{2f_{\mathrm{ax}}}{\delta_{\mathrm{gap}}}.$$

Therefore, in order to have a stable air gap, the structural stiffness of the housing must be higher than the *critical stiffness* k_c. For our motor, the maximum axial force is calculated as $f_{\mathrm{ax}} = 32\ \mathrm{kN}$ while the nominal air gap is $1.3\ \mathrm{mm}$ [13], which specifies the critical stiffness to be $k_c = 5 \times 10^7 \mathrm{N/m}$. To be on the safe side, the motor housing is designed such that the equivalent stiffness of the armature and housing k_{hous} is twice this critical value.

D. Bearings

Precision of a robot cannot be achieved even with a sophisticated controller if the mechanical parts of the system fail to operate precisely. In a direct-drive joint, the motor bearing set, which supports both rotor and robot arm, is the only moving part, and hence, the main source of mechanical imperfections such as tolerances or deflection. Moreover, without a gearbox, the bearing friction is the only source of joint friction. Therefore, the bearings must be chosen carefully in a suitable arrangement.

According to International Standard ISO 9283, two important robot performance criteria are path repeatability and distance repeatability. These are determined by how much of the hysteresis of each joint is caused by friction and the cumulative effect of bearing tolerances. The other relevant specification is static compliance, namely the maximum displacement of a robot's tip per unit of applied load on the robot's tip. Depending on the applications, the applied load can be any component of the generalized forces/moments. The tip displacement is determined by the combination of the joint controller, robot links, and bearing compliances. Since the robot control is usually based on joint angle sensing, the bearing deflection cannot be compensated by control. Hence, joint stiffness is another design consideration that adversely affects the positioning accuracy. The other design issue is that the bearing should be able to carry the required load while contributing only minimum weight.

Axial air gaps produce huge attraction forces, estimated to be up to $32\ \mathrm{kN}$ for our motor prototype, which can adversely affect friction and lifetime of the bearings. The major development in the new design is the use of double armature pairs to cancel out the reaction force [3]. To achieve this, we integrate two motors back-to-back such that the axial forces are taken by the motor's aluminum housing, as shown in Fig. 1(a). Each stator–rotor armature pair is a complete motor that can be assembled separately. This facilitates motor assembly and air gap adjustment. Moreover, an evaluation of several bearing configurations revealed that a centered bearing placement [Fig. 1(a)] is superior. Since the rotors are pivoted at the middle, the variation of both air gaps due to elastic deflection of the housing are altered equally, and the axial forces remain identical.

The next design step is selecting bearing type and size. Generally, the reaction forces on the bearings are due to external shear and axial forces, but primarily bending moments. Therefore, the bearing has to have desirable bending properties. Generally, bearing stiffness is determined by the type, size, and number of its balls or rollers. The heavier bearings are usually the stiffer ones; however, it is not desirable, especially for direct-drive robots. A thin-section bearing has a greater number of balls than a conventional bearing, which yields higher stiffness and load-carrying capability compared to a conventional bearing of the same weight [14]. Moreover, large-diameter bearings have high bending stiffness as the reaction forces on the rolling elements decrease with increasing diameter for a given moment. On the other hand, the tolerances do not increase as much with the diameter [14]. The friction torque at the bearing tends to increase with an increase in bearing bore diameter and radial load. Yet, since the reaction bearing force due to external bending

moment decreases with larger diameter, the friction does not depend on the size of bearing. In short, thin-section bearings save both space and weight and a larger bearing diameter is desirable, of course within the limitation of cost and geometrical feasibility. Finally, a pair of *thin-section angular contact ball bearings* (Kaydon KD100ARO) with $254\ \mathrm{mm}$ inside diameter was chosen. The bearings are mounted back-to-back to achieve high stiffness $(2.5 \times 10^7\ \mathrm{N{\cdot}m/rad})$, and they come with prespecified medium-duty payload.

E. Torque Sensor

1) Design: The application of *joint-torque sensory* feedback (JTF) in robot control to suppress the effect of load torque on a motion servo controller has been proposed [8], [9], [15], [16]. This control scheme, unlike the *model-based controllers*, does not require the dynamic model of the load, i.e., the links of a manipulator. However, JTF assumes precise measurement of joint torque, which, in practice, encounters several design challenges. Various techniques have been proposed to instrument a motor for torque sensing by cementing strain gauges either to the motor's hub [17]–[22], to its transmission [17], [19], [23], [24], or to its shaft [19], while little attention has been paid to find an adequate structure for joint torque sensing [10], [20]. Typically, in the design of a mechatronics system, it is desirable that much of the torque/force reaction of the load on the motor shaft appears in the form of nontorsional components, because actuation then takes less effort. In robotics, for instance, the SCARA arm design prevents gravity torques from acting on the joint motors. However, since torque sensors are directly attached to the motor's distal links, they have to bear those potentially large nontorsional components. The first challenge is to measure torque with minimal influence from simultaneous and potentially large nontorsional components. The second challenge relates to the sensor stiffness. High torsion stiffness is important because any deflection adds positioning errors that cannot be compensated by the joint servo controller. To increase the SNR and sensitivity of the sensor, it is desirable to design a structure that generates a large strain for a given load torque. However, the sensitivity introduces a torsion compliance that must be minimized. Thus, there are two conflicting requirements: high stiffness and high sensitivity for torsion. Furthermore, minimizing the effects of thermal stresses is a design factor that cannot be ignored; the motor is a source of heat that flows from the motor to the attached load through the sensor body. Therefore, it is desirable to have an axis-symmetric design that constrains the heat to flow in the axial direction, where no position constraint usually exists.

The *hollow-hexaform* design of torque sensor satisfies these requirements [10]. Fig. 4 illustrates the torque sensor prototype that is specifically designed and built for a flange mounting to the motor's hollow shaft. Note that the sensor body is machined from a solid piece of metal, i.e., *monolithic structure*, to decrease the hysteresis and increase the strength and repeatability of the sensor.

2) Sensor Characteristics: The sensor output versus torque is plotted in Fig. 5(a). The maximum deviation from linearity is 0.2% full scale. Fig. 5(b) shows the frequency response of the sensor flanged to a massive steel disk, revealing two distinct modal frequencies that belong to torsion and bending modes. The corresponding torsion and bending stiffnesses are 2.4×10^5 and $4.8 \times 10^6\ \mathrm{N{\cdot}m/rad}$, respectively. Moreover, with a measured cross sensitivity of 0.6%, the sensor can tolerate extensive nontorsional force/moment components.

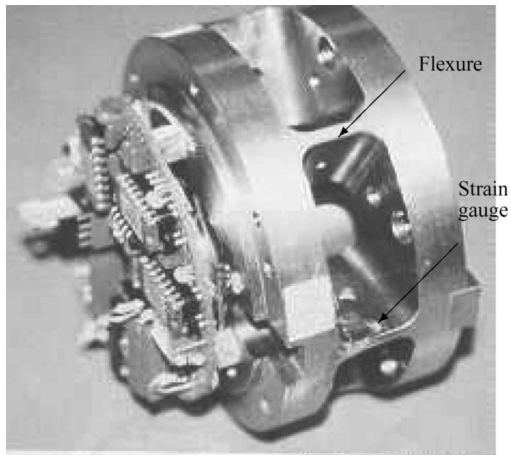

Fig. 4. Torque sensor prototype.

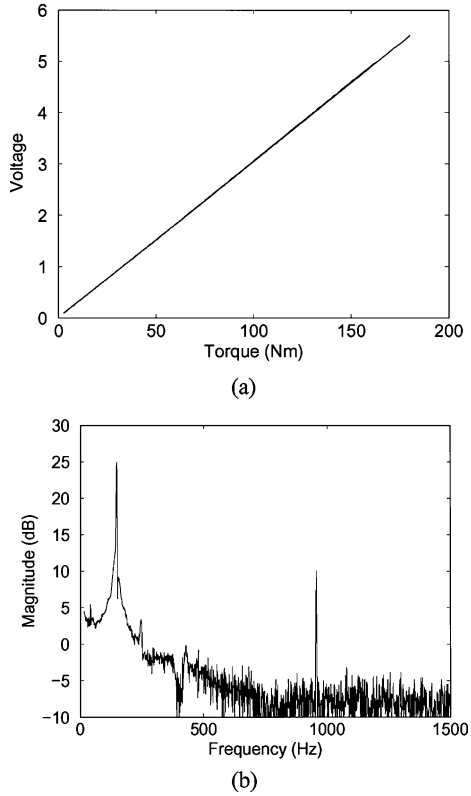

Fig. 5. Characteristics of the torque sensor. (a) Sensor output versus applied torque. (b) Dynamic response.

III. Dynamometer

The dynamometer was designed to serve several experiments. For the motor torque calibration test, the motor velocity must be

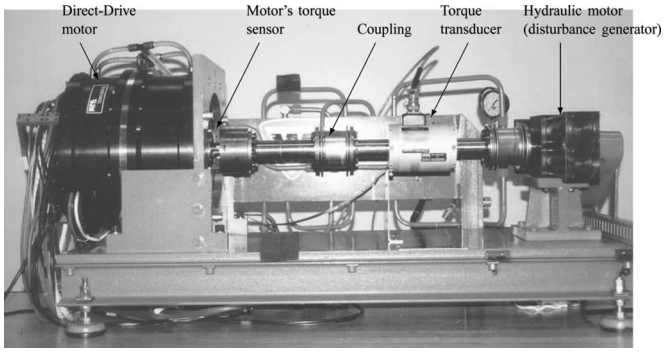

Fig. 6. Motor prototype mounted on the dynamometer.

regulated independent of motor torque while for the disturbance sensitivity test [9], a random torque must be generated, requiring an active load. The major design problem was the selection of an appropriate actuator for the active load. It has to be powerful enough to overcome the direct-drive motor torque and has to operate in both velocity and torque control modes. Hydraulic actuators are well suited for this task. They are powerful and can be commanded under velocity control simply via flow control valves.

Fig. 6 illustrates the motor prototype mounted the dynamometer. The direct-drive motor and a hydraulic rack and pinion rotary motor (Parker 113A129BME) are mounted on the rigid base of the dynamometer. The hydraulic motor's shaft is connected to that of the direct-drive motor via a reference torque transducer (Himmelstein SHC2804TC) by means of two couplings (Gam/Jakob KSS-450).

In *velocity mode*, the speed of the hydraulic motor is controlled by two pressure-compensated flow control valves (Parker TPCS600S01 and TPCS600S6), which can regulate the angular speed from $1\,^{\circ}/\mathrm{s}$ for quasi-static test to 1 r/s. An adjustable cam and two limit switches detect the two rotational extremes and activate a solenoid valve (Parker D1VW1CJ) through a PLC unit to reverse the direction of the rotation accordingly. In *torque mode*, the hydraulic motor must generate pseudorandom torque disturbances and we use a solenoid directional valve to produce a time-varying torque. The hydraulic pressure is regulated by using a flow-compensated pressure-regulator value in order to have contact magnitude pertaining to the torque generated by the hydraulic motor.

IV. Control

A. Control Configuration

Fig. 7 illustrates the block diagram of the control system that consists of three complementary subsystems:

1) motor torque controller that minimizes torque ripple and power losses while it increases the maximum torque capacity of the motor with respect current/magnetic saturation;
2) position control system;
3) optimal joint torque feedback that minimizes the effect of external disturbance or load torque on the motion control system.

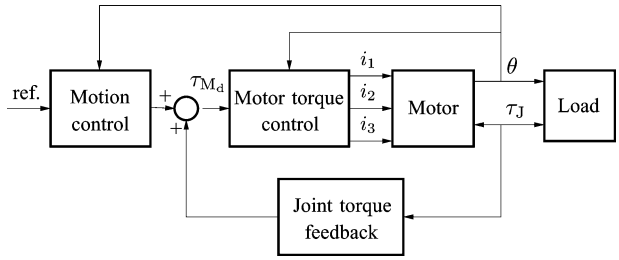

Fig. 7. Configuration of the control system.

These controllers will be described separately in the following sections.

B. Motor Torque Control

1) Control Design: Direct-drive brushless motors are ideal applications where precise position tracking is critical. They can, in principle, substantially improve the positioning precision since they lack the gears required in conventional electric drive systems. However, by the same token, direct-drive systems are more adversely affected by the motor's torque ripple. Moreover, direct-drive motors suffer from relatively low torque capability, which is limited by power loss and magnetic saturation. Ideally, a torque controller needs to solve three tasks: minimize torque ripple, minimize copper losses (recall that the lower the dissipation, the higher the continuous torque), and maximize the torque capability by taking magnetic saturation and current limitations into account. Such a controller is briefly described in this section. Control approaches for accurate torque production in direct-drive systems and their underlying models have been studied by several researchers [6], [12], [25]–[28]. The control problem is radically simplified when the motor's phase currents are considered as the inputs. Then the torque control problem, also known as the commutation law, is how to modulate the current phases as a function of position θ such that the desired set-point torque $\tau_{\mathrm{M_d}}$ is generated.

Fig. 8 illustrates the torque control system that comprises three functional elements: brushless motor, current amplifiers, and the electronic torque controller. We assume that there is negligible cross-coupling between the phase torques and there is no reluctance torque. In addition, we assume that the phase currents can be controlled accurately and instantaneously so that the phase currents can be treated as the control inputs. The motor torque τ_{M} is the superposition of the torque contributions of p phases

$$\tau_{\mathrm{M}} = \sum_{j=1}^{p} i_j(\theta, \tau_{\mathrm{M_d}}) a_j(\theta) \tag{3}$$

where i_j is the current of the jth phase, θ is the shaft angle, and $a_j(\theta)$ is the position nonlinearity associated with the jth phase. For brevity, we shall omit the argument θ in the following.

The torque control problem is to solve the previous equation in terms of current $i_j(\theta, \tau_{\mathrm{M_d}})$ as a function of motor position, given a desired motor torque $\tau_{\mathrm{M_d}}$. Given a scalar torque set point, (3) permits infinitely many (position dependent) phase current waveforms. Since the continuous mechanical power output

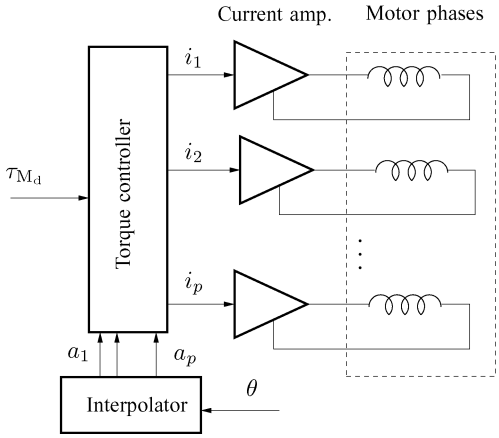

Fig. 8. Torque controller and power electronics.

of electrical motors is limited primarily by heat generated from internal copper losses, it makes sense to use the freedom in the phase current solutions to minimize power losses P that is proportional to $i^T i$, where vector $i \in \mathbb{R}^p$ contains the phase currents. Current saturation is the other limitation that should be considered. Let $i_{\max} < 0$ be the maximum equivalent phase current corresponding to existing a linear phase current–torque relationship, i.e., (3) is valid, or to current limit of the servo-amplifier. Then, the phase currents must satisfy $|i_j| \leq i_{\max}\ \forall j = 1, \ldots, p$.

In order to derive the optimal phase currents $i_j^*(\theta, \tau_{\mathrm{M_d}})$ that generate the desired torque (3) and minimize the power losses subject to the constraints, we need the torque functions $a_j(\theta)$. Let the functions be represented in a discrete manner at a finite number of motor positions. Then, the values of the functions at any specific position θ, i.e., $a(\theta)^T = (a_1(\theta), \ldots, a_p(\theta)]$, can be interpolated. Hereafter, we drop the argument θ for simplicity. Now, by setting $\tau_{\mathrm{M}} = \tau_{\mathrm{M_d}}$ in (3), the problem of finding optimal phase currents that minimize power losses subject to the constraints is formulated by the quadratic programming problem,

$$\min i^T i \tag{4}$$

$$h(i) = a^T i - \tau_{\mathrm{M_d}} = 0 \tag{5}$$

$$g_j(i) = |i_j| - i_{\max} \leq 0, \qquad j \in \mathcal{J}. \tag{6}$$

Since all the functions are convex, any local minimum is a global minimum as well. Now, we seek the minimum point $i^* \in \mathbb{R}^p$ satisfying the equality and inequality constraints.

Defining the function

$$\mathcal{L}(i) = f(i) + \lambda h(i) + \mu^T g(i) \tag{7}$$

where $f(i) = i^T i, g(i) = [g_1(i), g_2(i), \ldots, g_n(i)]^T \in \mathbb{R}^p, \lambda \in \mathbb{R}$, and $\mu = [\mu_1, \mu_2, \ldots, \mu_n]^T \geq 0 \in \mathbb{R}^p$, the optimal point can be found by using the Kuhn–Tucker theorem [29]. Let i^* provide a local minimum of $f(i)$ satisfying the equality and inequality constraints $h(i)$, then $\partial\mathcal{L}/\partial i|_{i=i^*} = 0$ and $\mu^T g(i^*) = 0$. Therefore,

$$2i^* + \lambda a + \mu^T \mathrm{sgn}(i^*) = 0 \tag{8}$$

$$\mu_j(|i_j^*| - i_{\max}) = 0, \quad j \in \mathcal{J} \tag{9}$$

where $\mathrm{sgn}(\cdot)$ represents the sign function. Equations (8) and (9) together with (5) constitute a set of $2p + 1$ nonlinear equations with $2p + 1$ unknowns i^*, λ, and μ to be solved in the following. Since $\mu^T g(i^*) = 0$ while $\mu \geq 0$ and $g(i^*) \leq 0$, we can say that $\mu_i = 0$ for $|i_j| > i_{\max}$, and that $\mu_j \geq 0$ for $|i_j| = i_{\max}$. Therefore, (8) can be written in the following compact form:

$$i_j^* = \mathrm{sat}(-0.5\lambda a_j), \qquad j \in \mathcal{J} \tag{10}$$

where

$$\mathrm{sat}(x) = \begin{cases} x, & |x| \leq i_{\max} \\ \mathrm{sgn}(x) i_{\max}, & \text{otherwise} \end{cases} \tag{11}$$

is the *saturation function*. This equation implies that the larger the magnitude of the torque shape function $|a_j|$, the larger the magnitude of the optimal current i_j^*. If the phases are labeled in descending order, the optimal phase currents from i_1^* to i_p^* must be saturated consecutively. In case saturation of a phase occurs, (10) implies that only knowing the sign of λ is enough to calculate the associate phase current. Therefore, if i_1^* saturates, then

$$i_1^* = \mathrm{sgn}(-a_1\lambda) i_{\max} = \mathrm{sgn}(a_1 \tau_{\mathrm{M_d}}) i_{\max}. \tag{12}$$

If i_1^* does not saturate, i.e., $|i_1^*| > i_{\max}$, then neither does $\{i_2, \ldots, i_p\}$. Let $\lambda^{(1)}$ represents the Lagrangian multiplier when i_1^* does not saturate, then

$$\lambda^{(1)} = \frac{-2\tau_{\mathrm{M_d}}}{a^T a} \tag{13}$$

which, in turn, can be substituted in (10) to obtain the optimal phase current

$$i_1^*(\theta, \tau_{\mathrm{M_d}}) = \mathrm{sat}\left(\frac{\tau_{\mathrm{M_d}}}{a(\theta)^T a(\theta)} a_1(\theta)\right). \tag{14}$$

Since the denominator in (14) is always positive, by virtue of (12), one can infer that (12) provides the optimal solution for the saturation case as well. Analogously, i_2^* can be calculated if $a_1 i_1^* - \tau_{\mathrm{M_d}}$ is treated as the known variable. In general, the ith phase current can be calculated by induction as follows: since up to $(i-1)$th phase currents have been already solved, we have

$$a_i i_i^* + \cdots + a_n i_p^* = \tau_{\mathrm{M_d}} - (a_1 i_1^* + \cdots + a_{i-1} i_{i-1}^*). \tag{15}$$

The Lagrangian multiplier associated with the case of unsaturated i_i^* can be found from (10) and (15) as

$$\lambda^{(i)} = \frac{-2(\tau_{\mathrm{M_d}} - \sum_{k=1}^{i-1} a_k x_k^*)}{a^T a} \tag{16}$$

which can be substituted into (10) to give

$$i_i^*(\theta, \tau_{\mathrm{M_d}}) = \mathrm{sat}\left(\frac{\tau_{\mathrm{M_d}} - \sum_{k=1}^{i-1} a_k i_k^*}{a^T a} a_i\right), \qquad i = 2, \ldots, p. \tag{17}$$

Equations (14) and (17) are the optimal phase currents, which produce the desired torque precisely, while minimizing power losses, subject to the constraints of current saturation.

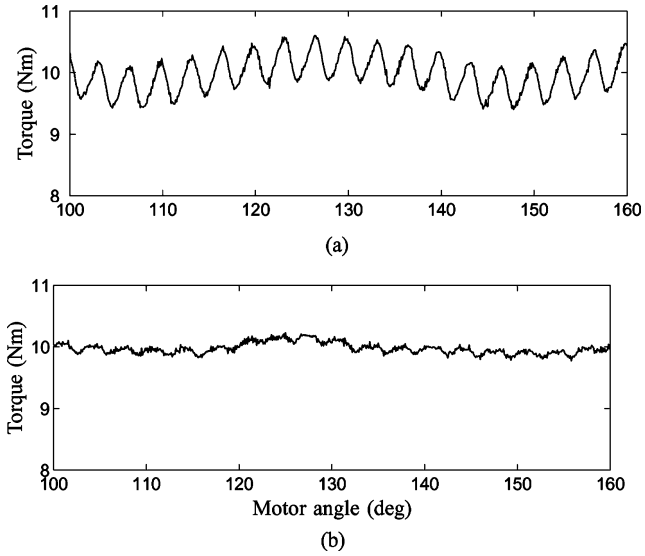

Fig. 9. Motor torque. (a) Sinusoidal commutation. (b) Optimal commutation.

Assume that vector $[a_j(\theta_1), a_j(\theta_2), \ldots, a_j(\theta_p)] \in \Re^p$ represents the discrete torque shape functions corresponding to p measurements of the phase torque (with unit current excitation) and positions. Then, at any given position θ, the corresponding shape function $a_j(\theta)$ can be calculated via interpolation. The torque control algorithm is implemented as follows.

1) Interpolate the torque functions $a_1, \ldots, a_p$ for the current motor position θ.
2) Set $i_j^* = 0$ for $a_j = 0$ (or for sufficiently small $|a_j|$). Pick the set of nonzero shape functions and sort them such that $|a_1| \geq |a_2| \geq \cdots \geq |a_p|$.
3) Calculate the optimal currents from (14) and (17). Go to step 1).

2) Experiment Results: We measure the torque shape functions by using the hydraulic dynamometer. To this end, the torque trajectory data versus position was registered during the rotation, while one phase was energized with a constant current.

The torque controller was tested on the dynamometer. Again, the motor shaft is rotated by the hydraulic actuator while the motor torque is monitored by the torque transducer. Fig. 9(a) and (b) shows the motor torque versus position when standard sinusoidal commutation and our torque controller are applied. Clearly, a drastic reduction in torque ripple is achieved.

A motor's torque ripple acts as a perturbation to the control system, degrading the tracking performance, especially at low velocities. We examine the position-tracking accuracy of our direct-drive system with and without torque ripple. To this end, a PID position controller is implemented, in addition to the torque controller. Fig. 10(a) and (b) documents the tracking error of the system to a ramp input, which is equivalent to a step input velocity of $20^\circ/\mathrm{s}$, when the sinusoidal commutation and our controller are applied, respectively. The figures clearly show that the tracking error is limited by the torque ripple. In case the proposed torque controller is applied, the tracking error is reduced down to 0.003°, which is about the encoder resolution (0.001°).

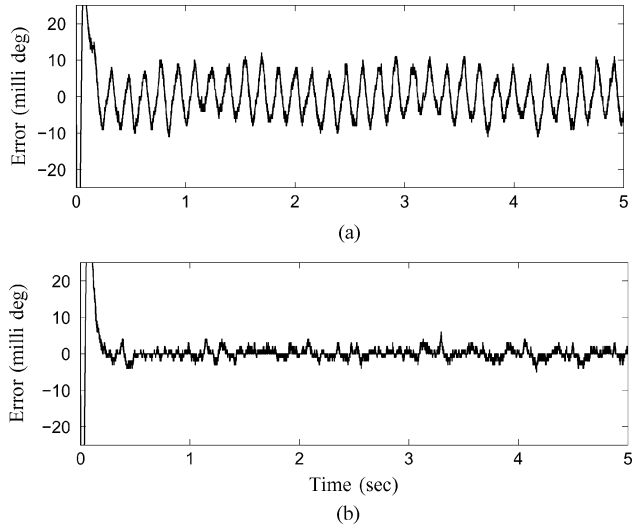

Fig. 10. Position-tracking error with respect to the ramp input. (a) Sinusoidal commutation. (b) Optimal commutation.

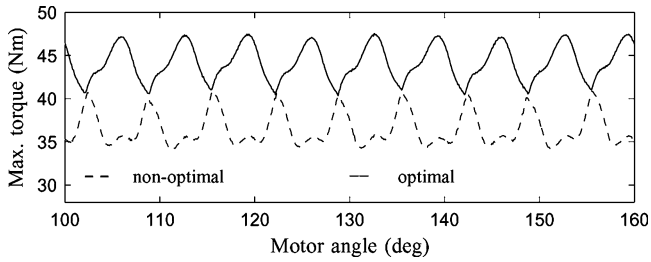

Fig. 11. Maximum torque corresponding to the current saturation.

By how much does the proposed controller improve the maximum torque capability of our motor prototype? Fig. 11 shows the graphs of the maximum achievable torque with respect to maximum phase current $i_{\max} = 15\mathrm{A}$ that are with (solid line) and without (dashed line) the consideration of the current saturation in the torque control law. Since only the lowest torque value is available over all motor positions, it is evident from the graphs that the motor torque limits corresponding to the torque controllers are 34 and $41\ \mathrm{N}\cdot\mathrm{m}$—an increase of 20%.

C. Motion Control With Joint Torque Feedback

Joint torque feedback simplifies greatly the motion control system by eliminating the dynamics of the load attached to the motor. A survey of JTF can be found in [16]. In summary, the main advantages claimed for JTF [8], [15] are as follows.

1) Joint sensory feedback simplifies greatly the complexity of system dynamics by eliminating the load dynamics, e.g., the links of a manipulator.
2) The control system is inherently robust with respect to parameter variation, e.g., a manipulator grasping a payload with mass variation.
3) The control system can completely reject external force disturbances applied on the load.

In robotics applications, joint torque sensing can be used to eliminate completely the effect of link dynamics if the

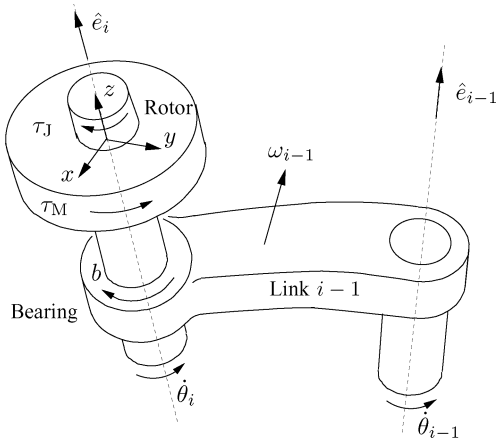

Fig. 12. ith joint.

manipulator's joint are endowed with joint torque sensor device [8], [9], [15], [16]. The system dynamics are determined completely by the motion of the motor rotors in the Cartesian space that is not detectable by the torque sensors.

Consider a robot with n revolute joints. Fig. 12 depicts the ith axis of such a robot, where the motor shaft is cut right at its junction to the next link. In the following, the subscript i denotes quantities related to the ith link or joint. Let ω_{z_i} be the z-component of the absolute angular velocity of the rotor ω_i; θ_i and J_i denote the rotor angle and the rotor inertia along the z-axis; and $\tau_{{\rm M}_i}, \tau_{{\rm J}_i}$, and $b_i(\dot{\theta})$ denote the torques of the motor, joint, and bearing friction, respectively. Assuming that the rotors are axisymmetric, i.e., their inertias about x- and y-axes are identical, and that they are statically balanced, i.e., their center of mass coincident with rotation axis, the equation of motion of the ith rotor is simply described by

$$J_i\dot{\omega}_{z_i} + b_i(\dot{\theta}_i) = \tau_{{\rm net}_i} \tag{18}$$

where

$$\tau_{{\rm net}_i} = \tau_{{\rm M}_i} - \tau_{{\rm J}_i}$$

is the net torque acting on the rotor. Since both the components of the net torque are known, we only need to obtain an expression for the absolute angular velocity in terms of joint angle quantities. Let $\hat{e}_j \in \mathbb{R}^3$ represent a unit vector in the direction of the jth joint axis. Then, assuming the deformation of the torque sensors is negligible, the link velocities can be computed by a technique similar to that described by Luh *et al*. [30]

$$\omega_{i-1} = \sum_{j=1}^{i-1} \hat{e}_j\dot{\theta}_j \tag{19}$$

$$\omega_{z_i} = \hat{e}_i^T\omega_{i-1} + \dot{\theta}_i. \tag{20}$$

Equations (19) and (20) can be combined in the vectorial form as

$$\omega_z = D(\theta)\dot{\theta} \tag{21}$$

where $D(\theta) \in \mathbb{R}^{n\times n}$ is a lower triangular matrix whose elements are

$$d_{ij} = \begin{cases} \hat{e}_i^T\hat{e}_j, & \text{if} \quad i \geq j \\ 0, & \text{otherwise.} \end{cases}$$

Defining $J = {\rm diag}\{J_i\}$ and using (21) in (18), we get

$$JD\ddot{\theta} + J\dot{D}\dot{\theta} + b(\dot{\theta}) = \tau_{\rm net}. \tag{22}$$

It is worth pointing out that the unit vectors $\hat{e}_j$s form the columns of the manipulator's Jacobian [31], i.e., $A_\omega := \partial\omega_n/\partial q = [\hat{e}_1 \quad \hat{e}_2 \quad \cdots \quad \hat{e}_n]$, and hence, the D matrix can be constructed from the Jacobian by

$$D = {\rm tri}(A_\omega^T A_\omega)$$

where function ${\rm tri}(\cdot)$ returns a matrix whose upper triangular elements are zero and the rest of its elements are equal to the corresponding elements of the input matrix. Now, the following *inverse-dynamics control* scheme:

$$\begin{aligned} \tau_{\rm M_d} &= \tau_{\rm J} + u \\ u &= JD\left(\ddot{\theta}_{\rm d} + G_{\rm D}(\dot{\theta}_{\rm d} - \dot{\theta}) + G_{\rm P}(\theta_{\rm d} - \theta)\right) + J\dot{D}\dot{\theta} + b \end{aligned} \tag{23}$$

where $G_{\rm D} < 0$ and $G_{\rm P} < 0$ are the PD gains, can achieve dynamic tracking of the desired trajectory $\theta_{\rm d}$.

D. Joint Torque Feedback in the Presence of Actuator Dynamics

1) Control Design: Ideally, positive joint torque feedback decouples the load dynamics exactly and provides infinite stiffness for external torque disturbance. This is because the torque feedback trivially compensated as an ideal actuator reproduces the same torque. However, in practice, due to the actuator's finite bandwidth dynamics, the feedback system may not respond fast enough to the load torque. As a result, a complete compensation of disturbance torque cannot be achieved in the presence of actuator dynamics and/or delay. This section presents an optimal filter for positive joint torque feedback control that takes the actuator's dynamics into account and minimizes, in the $\mathcal{H}_\infty$ sense, the sensitivity to load torque disturbance [9]. We show that finding the optimal torque feedback is equivalent to the model-matching problem that has an exact solution [32]. In the case of a dynamic load, optimal torque feedback minimizes the effect of load perturbation on the nominal rotor dynamics. A single variable case is considered herein, yet the analytic solution can be readily extended for a multivariable case.

The general block diagram is shown in Fig. 13 where transfer function $H(s)$ represents the actuator dynamics; note that, for an ideal actuator, $H(s) \equiv 1$. The external disturbance $\tau_{\rm J}$ is measured via a torque sensor between the rotor and the load and is fed back for compensation through a filter $Q(s)$. Let $u(s)$ be the compensated control input under positive joint torque feedback in the Laplace domain. Then, (23) is rewritten as

$$\tau_{\rm M_d}(s) = u(s) + Q(s)\tau_{\rm J}(s) \tag{24}$$

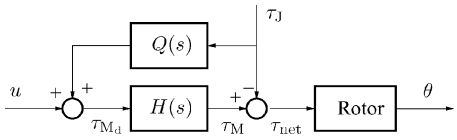

Fig. 13. Joint torque feedback through filter $Q(s)$.

and s is the Laplace variable. The disturbance sensitivity function

$$\chi(s) := \frac{\tau_{\rm net}(s)}{\tau_{\rm J}(s)} = -1 + H(s)Q(s) \tag{25}$$

shows how the disturbance $\tau_{\rm J}(s)$ is transmitted to the net torque $\tau_{\rm net}(s)$ acting on the rotor. Also, let $G(s)$ represent the compliance of a position feedback controller, i.e.,

$$G(s) = \left.\frac{\partial\theta(s)}{\partial\tau_{\rm J}(s)}\right|_{Q=0}.$$

Then, it can be shown [9] that the addition of the JTF loop changes the overall compliance of the motion servo to

$$G_{\rm JTF}(s) = \chi(s)G(s)$$

which is equivalent to the weighted disturbance function, if the weighting function is chosen as $W_1(s) = |G(s)|/\|G\|_\infty$. Now, the problem is to find a stable and realizable filter $Q(s) \in \mathcal{RH}$ (the class of $\mathcal{H}_\infty$ functions that are rational) such that the maximum weighted sensitivity of the system is minimized, which is

$$\inf_{Q(s)\in\mathcal{RH}} \left\| \left[\frac{W_1(1-HQ)}{W_2Q}\right] \right\|_\infty. \tag{26}$$

Note that the first weighting function $W_1(s)$ shapes the disturbance gain over a frequency band of interest, while the second weighting function $W_2(s)$ shapes the magnitude of the optimal filter $Q(s)$. Note that $W_2(s)$ causes the magnitude of the torque filter $Q(s)$ to roll off at high frequency where the magnitude of $W_1(s)$ is sufficiently low. Equation (26) is a standard $\mathcal{H}_\infty$ problem and the optimal solution is available [9], [32], [33].

2) Position Controller: For the joint torque feedback to be effective requires an accurate measurement of the joint torque. However, the torque sensor's gain and offset are prone to change due to temperature variation. In the course of our experiments, it became evident that joint torque feedback introduces a bias in position tracking due to the torque sensor offset. An adaptive version of JTF that requires only uncalibrated joint torque sensing and can tune the gain and the offset of the sensor is presented in [34]. Nevertheless, there is a simpler solution that can deal with the problem of the sensor offset. The sensor bias acts as a constant disturbance on the position controller resulting in a steady-state error. The error can be eliminated if the position controller has an integral action, i.e., using a PID position controller. In our application, a PID position controller is used whose gains are tuned as the following: $G_{\rm P} = 40\,{\rm N\cdot m/^\circ}$, $G_{\rm I} = 200\,{\rm N\cdot m/^\circ\cdot s}$, and $G_{\rm D} = 0.8\,{\rm N\cdot m\cdot s/^\circ}$.

Since the motor does not have any sensor to measure the joint velocity, it has to be estimated from the encoder measurement. Different estimators have been proposed for precise estimation of the velocity, which can be found, for example, in [35] and [36]. Herein, we obtain an approximate differentiation of the position measurement by using the causal filter $s/(\sigma s+1)$, where $\sigma \ll 1$; we select $\sigma = 0.05$ s in our application.

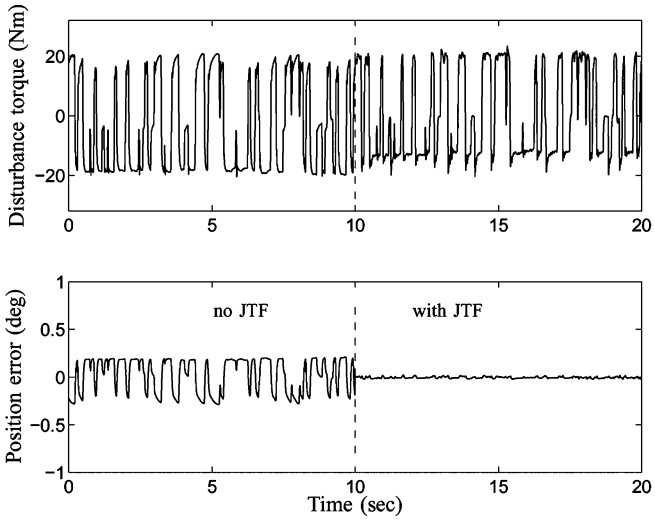

Fig. 14. Tracking error without and with JTF applied.

3) Experimental Results: In order to measure the torque disturbance sensitivity, torque disturbances are injected into the direct-drive system by the hydraulic dynamometer. We commanded a ramp reference signal through the PID position controller while the hydraulic motor-injected random torque disturbances. The performance of joint torque feedback critically relies on the knowledge of actuator dynamics, which, in turn, can be obtained from disturbance sensitivity tests. Let us consider the control system shown in Fig. 13. The challenge in identifying system $H(s)$ is that signal $\tau_{\rm M}$ is not measurable. However, the transfer function can be extracted from measurements of the disturbance sensitivity function with two different feedbacks. By denoting $G'_{\rm JTF}$ as the sensitivity function corresponding to $\chi \equiv 1$, one can obtain $G'_{\rm JTF}(s) = (H(s)-1)G(s)$ from (25). Let us assume that $\Phi_{\tau_{\rm J}\tau_{\rm J}}$ and $\Phi_{\theta\tau_{\rm J}}$ denote the power spectral density and the cross-correlation spectral density related to measured signals $\tau_{\rm J}$ and θ when $Q=0$, and that $\Phi'_{\tau_{\rm J}\tau_{\rm J}}$ and $\Phi'_{\theta\tau_{\rm J}}$ denote the corresponding spectral densities when $Q=1$. Then, one can obtain the empirical (nonparametric) transfer function $\hat{H}(\omega)$ via [9]

$$\hat{H}(j\omega) = 1 + \frac{\Phi_{\theta\tau_{\rm J}}(j\omega)\Phi'_{\tau_{\rm J}\tau_{\rm J}}(j\omega)}{\Phi'_{\theta\tau_{\rm J}}(j\omega)\Phi_{\tau_{\rm J}\tau_{\rm J}}(j\omega)}. \tag{27}$$

The next step of the identification involves a numerical procedure to represent the complex function (27) by a rational transfer function as close as possible. Several parametric models were examined, and it turned out that a second-order system is sufficient to match the input–output behavior adequately. The parametric model approximating $H(s)$ is

$$\hat{H}(s) \approx \frac{-5.014s + 578}{s^2 - 35.59s + 604}.$$

Fig. 14 illustrates the position-tracking error trajectories due to the random torque disturbances without and with the torque

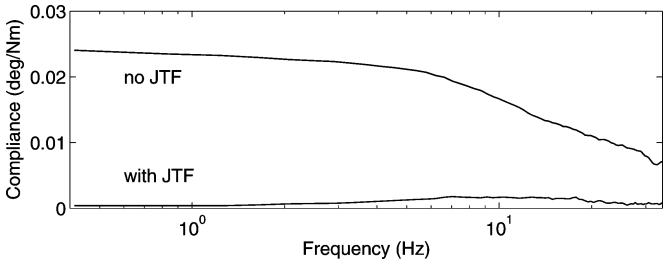

Fig. 15. Experimental disturbance attenuation with and without JTF applied.

TABLE I
STIFFNESS OF DIFFERENT JOINT COMPONENTS

	torsion stiffness Nm/rad	bending stiffness Nm/rad
motion control	4.8×10^4	-
torque sensor	2.4×10^5	4.8×10^6
joint bearings	-	2.5×10^7

feedback applied. The control system exhibits relatively high disturbance sensitivity when there is no torque feedback. The figure clearly shows that the tracking error is substantially reduced when the torque feedback is applied. The disturbance attenuation is better explained in Fig. 15 in the frequency domain. As expected, at a sufficiently high frequency, the disturbance sensitivity drops due to the attenuation effect of position feedback. The torque feedback lowers this system sensitivity remarkably over the whole frequency range. It is worth noting that, since the actuator and position sensor are colocated, the joint angle is slightly different from the sensed angle, depending on the torsional stiffness of the torque sensor. Moreover, the bending deflection of the sensor and of the joint bearings add uncertainty in positioning accuracy. Table I lists the stiffness of different joint components, where the stiffness of the control system is at the lowest.

To demonstrate the system's ability to reject unknown load torques, a link with a 7.2-kg body mass is mounted on the motor's torque sensor that plays the role of an uncertain payload. In this experiment, the counterbalance weight is fixed at distances $240, 350$, and 480 mm off the center in order to establish three load cases each of which with different inertia and gravity torque, as specified in Table II. To investigate the tracking performance of the control system, we commanded a sinusoidal reference position trajectory $\theta_{\rm d}(t) = 3 + \pi/4 \cos(\pi t/3)$ rad to the motion controller. First, no JTF is applied. Since the nonlinear link dynamics (due to the gravitational term) are not compensated by a JTF controller, the tracking errors resulting from the PID controller alone are large for all load cases, as shown in Fig. 16. Yet, when the joint torque feedback is applied, the tracking errors are reduced significantly. The plots also demonstrate the robustness of JTF with respect to variation of the load; the servo controller with JTF applied achieves excellent position tracking for all load cases.

V. CONCLUSION

The design and control of a high-performance direct-drive system suitable for robotics and automation were presented. The key elements of the design are as follows.

TABLE II
INERTIAL PROPERTIES OF THE LOADS

load case	max. gravity Nm	inertia kgm^2
1	24.2	0.7
2	30.5	1.1
3	39.7	1.9

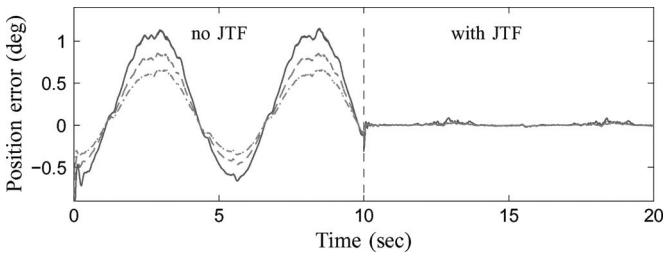

Fig. 16. Position errors with different load case: dashed-dotted, dashed, and solid lines are associated with the first, second, and third load cases, respectively.

1) The actuator is axial air-gap synchronous that is built in a dual configuration, i.e., two pairs of rotor and stator.
2) A special bearing arrangement maximizes the joint stiffness with respect to bending $(2.5 \times 10^7\ {\rm N\cdot m/rad})$ and leads to minimum joint friction.
3) The thermal characteristics of the motor have been substantially improved by placing a system of cooling-water tubes in the proximity of the armature coils and using a thermoconductive epoxy. Experiments showed that the thermal resistance, and hence, the continuous torque capacity of the motor, was improved by a factor of 6.

i) The torque sensor was integrated to the motor. The sensor's key features are its extremely high stiffness—torsion stiffness $2.4 \times 10^5\ {\rm N\cdot m/rad}$ and bending stiffness $4.8 \times 10^6\ {\rm N/rad}$—as well as insensitivity to all exogenous torque/force components that makes it suitable for joint torque sensing.

A hydraulic dynamometer has been designed and constructed to work in velocity and torque control modes for calibration of the motor and for various performance tests.

The overall control system consists of three complementary subsystems: motor torque control, motion control, and JTF. More specifically, we have shown the following.

1) We presented the explicit solution to the motor-torque control problem with copper losses as the cost function while the torque equation and magnetic (or current) saturation enter as equality and inequality constraints. Experimental results showed that torque-ripple is almost eliminated (about $\pm 1.5\%$), and that is essential for precise motion tracking; the ripple-free torque controller reduced the position-tracking error with respect to a ramp input of 0.003°. We also showed that the optimal torque controller enhances the maximum torque capability of the motor by 20%.
2) An $\mathcal{H}_\infty$ positive joint torque feedback was presented, which incorporates the torque sensor signal and optimally suppresses the effect of load torque disturbance on the motion control system in the presence of actuator dynamics.

The experimental results illustrated that a significant improvement in torque disturbance rejection and load decoupling was achieved; the worst case sensitivity to torque disturbance was reduced to $0.0012^{\circ}/\mathrm{Nm}$.

REFERENCES

[1] C. H. An, C. G. Atkeson, and J. M. Hollerbach, *Model-Based Control of a Robot Manipulator*. Cambridge, MA: MIT Press, 1988.

[2] H. Asada and K. Youcef-Toumi, *Direct-Drive Robots*. London, U.K.: MIT Press, 1987.

[3] J. M. Hollerbach, I. Hunter, J. Lang, S. Umans, and R. Sepe, "The McGill/MIT direct drive motor project," in *Proc. IEEE Int. Conf. Robot. Autom.*, 1993, pp. 611–617.

[4] J. M. Hollerbach, I. W. Hunter, and J. Ballantyne, "A comparative analysis of actuator technologies for robotics," in *The Robotics Review 2*, O. Khatib, J. Craig, and T. Lozano-Perez, Eds. Cambridge, MA: MIT Press, 1991.

[5] R. Welburn, "Ultra high torque motor system for direct drive robotics," presented at the Motor Control Conf., Atlantic City, NJ, Apr. 1984.

[6] F. Aghili, M. Buehler, and J. M. Hollerbach, "Experimental characterization and quadratic programming-based control of brushless-motors," *IEEE Trans. Control Syst. Technol.*, vol. 11, no. 1, pp. 139–146, Jan. 2003.

[7] T. M. Jahns and W. L. Soong, "Pulsating torque minimizing techniques for permanent-magnet ac motor drives—A review," *IEEE Trans. Ind. Electron.*, vol. 43, no. 2, pp. 321–330, Apr. 1996.

[8] K. Kosuge, H. Takeuchi, and K. Furuta, "Motion control of a robot arm using joint torque sensors," *IEEE Trans. Robot. Autom.*, vol. 6, no. 2, pp. 258–263, Apr. 1990.

[9] F. Aghili, M. Buehler, and J. M. Hollerbach, "Motion control systems with H-infinity positive joint torque feedback," *IEEE Trans. Control Syst. Technol.*, vol. 9, no. 5, pp. 685–695, Sep. 2001.

[10] F. Aghili, M. Buehler, and J. M. Hollerbach, "Design of a hollow hexaform torque sensor for robot joints," *Int. J. Robot. Res.*, vol. 20, no. 12, pp. 967–976, 2002.

[11] F. Aghili, M. Buehler, and J. M. Hollerbach, "Development of a high performance joint," *Int. J. Adv. Robot.*, vol. 16, no. 3, pp. 233–250, 2002.

[12] F. Aghili, M. Buehler, and J. M. Hollerbach, "Optimal commutation laws in the frequency domain for PM synchronous direct-drive motors," *IEEE Trans. Power Electron.*, vol. 15, no. 6, pp. 1056–1064, Nov. 2000.

[13] MPB, "Telerobotic development systems preliminary design review: Prototype 1 direct drive actuator research robot project (tds-4), " MPB Technologies, Montreal, QC, Canada, Tech. Rep., 1993.

[14] R. F. George, "Evaluating bearing for robots," presented at the Conf. Mach. Des., Miami Beach, FL, Apr. 1983.

[15] M. Hashimoto, "Robot motion control based on joint torque sensing," in *Proc. IEEE Int. Conf. Robot. Autom.*, 1989, pp. 256–261.

[16] D. Stokic and M. Vukobratovic, "Historical perspectives and states of the art in joint force sensory feedback control of manipulation robots," *Robotica*, vol. 11, pp. 149–157, 1993.

[17] L. E. Pfeffer, O. Khatib, and J. Hake, "Joint torque sensory feedback in the control of a PUMA manipulator," *IEEE Trans. Robot. Autom.*, vol. 5, no. 4, pp. 418–425, Aug. 1989.

[18] C.-H. Wu, "Compliance control of a robot manipulator based on joint torque servo," *Int. J. Robot. Res.*, vol. 4, no. 3, pp. 55–71, 1985.

[19] J. Luh, W. Fisher, and R. Paul, "Joint torque control by a direct feedback for industrial robot," *IEEE Trans. Autom. Control*, vol. 28, no. 2, pp. 153–161, Feb. 1983.

[20] C. W. deSilva, T. E. Price, and T. Kanade, "Torque sensor for direct-drive manipulator," *ASME J. Eng. Ind.*, vol. 109, pp. 122–127, 1987.

[21] H. Asada and S.-K. Lim, "Design of joint torque sensors and torque feedback control for direct-drive arms," in *Proc. ASME Winter Annu. Meeting: Robot. Manufact. Autom., PED*, Miami Beach, FL, Nov. 1985, vol. 15, pp. 277–284.

[22] D. Vischer and O. Khatib, "Design and development of high-performance torque-controlled joints," *IEEE Trans. Robot. Autom.*, vol. 11, no. 4, pp. 537–544, Aug. 1995.

[23] M. Hashimoto, Y. Kiyosawa, and R. Paul, "A torque sensing technique for robots with harmonic drives," *IEEE Trans. Robot. Autom.*, vol. 9, no. 1, pp. 108–116, Feb. 1993.

[24] D. Vischer and O. Khatib, *Design and Development of Torque-Controlled Joints*. New York: Springer-Verlag, 1990.

[25] D. G. Manzer, M. Varghese, and J. S. Thorp, "Variable reluctance motor characterization," *IEEE Trans. Ind. Electron.*, vol. 36, no. 1, pp. 56–63, Feb. 1989.

[26] R. S. Wallace and D. G. Taylor, "Low-torque-ripple switched reluctance motors for direct-drive robotics," *IEEE Trans. Robot. Autom.*, vol. 7, no. 6, pp. 733–742, Dec. 1991.

[27] F. Filicori, C. G. L. Bianco, and A. Tonielli, "Modeling and control strategies for a variable reluctance direct-drive motor," *IEEE Trans. Ind. Electron.*, vol. 40, no. 1, pp. 105–115, Feb. 1993.

[28] D. G. Taylor, "Nonlinear control of electric machines: An overview," *IEEE Control Syst. Mag.*, vol. 14, no. 6, pp. 41–51, Dec. 1994.

[29] H. W. Kuhn and A. W. Tucker, *Nonlinear programmingProc. 2nd Berkeley Symp. Math. Stat. Probab.* Berkeley, CA: Univ. of California Press, 1951, pp. 481–492.

[30] J. Y. S. Luh, M. W. Walker, and R. P. Paul, "Resolved acceleration control of mechanical manipulator," *IEEE Trans. Autom. Control*, vol. 25, no. 3, pp. 468–474, Jun. 1980.

[31] L. Sciavicoo and B. Siciliano, *Modeling and Control of Robot Manipulator*, 2nd ed. New York: Springer-Verlag, 2000.

[32] B. Francis, *Lecture Notes in Control and Information Science*. New York: Springer-Verlag, 1987.

[33] C. Foias, B. Francis, J. Helto, H. Kwakernaak, and J. Pearson, *H Infinity Control Theory*. New York: Springer-Verlag, 1990.

[34] F. Aghili and M. Namvar, "Adaptive control of manipulators using uncalibrated joint-torque sensing," *IEEE Trans. Robot.*, vol. 22, no. 4, pp. 854–860, Aug. 2006.

[35] G. Liu, A. A. Goldenberg, and Y. Zhang, "Precise slow motion control of a direct-drive robot arm with velocity estimation and friction compensation," *Mechatronics*, vol. 14, pp. 821–834, 2004.

[36] P. R. Bélanger, "Estimation of angular velocity and acceleration from shaft encoder measurements," in *Proc. 1992 IEEE Int. Conf. Robot. Autom.*, Nice, France, May 1992, pp. 585–592.

Farhad Aghili (M'01–SM'07) received the B.Sc. degree in mechanical engineering and the M.Sc. degree in biomedical engineering from Sharif University of Technology, Tehran, Iran, in 1988 and 1991, respectively, and the Ph.D. degree in mechanical engineering from McGill University, Montreal, QC, Canada, in 1998.

During 1994–1997, he was a Research Engineer with MPB Technologies, Montreal. In January 1998, he joined the Canadian Space Agency (CSA), Saint-Hubert, QC, where he is currently a Research Scientist. He is also an Adjunct Professor in the Mechanical and Industrial Engineering Department, Concordia University, Montreal. His current research interests include robotics, control systems, and mechatronics systems.

John M. Hollerbach (M'85–SM'92–F'96) received the B.S. degree in chemistry and the M.S. degree in mathematics from the University of Michigan, Ann Arbor, in 1968 and 1969, respectively, and the S.M. and Ph.D. degrees in computer science from Massachusetts Institute of Technology (MIT), Cambridge, in 1975 and 1978, respectively.

John M. Hollerbach is Professor in the School of Computing, and Research Professor of Mechanical Engineering, at the University of Utah. From 1989–1994 he was the Natural Sciences and Engineering/Canadian Institute for Advanced Research Professor of Robotics at McGill University, jointly in the Departments of Mechanical Engineering and Biomedical Engineering. From 1982–1989 he was on the faculty of the Department of Brain and Cognitive Sciences and a member of the Artificial Intelligence Laboratory at MIT; from 1978–1982 he was a Research Scientist. He received his BS in chemistry ('68) and MS in mathematics ('69) from the University of Michigan, and SM ('75) and PhD ('78) from MIT in Computer Science.

In 1984 he received an NSF Presidential Young Investigator Award, in 1988 he was named a Fellow of the Canadian Institute for Advanced Research, and in 1996 he became an IEEE Fellow. He was the Program Chairman of the 1989 IEEE International Conference on Robotics and Automation, a member of the Administrative Committee of the IEEE Robotics and Automation Society from 1989–1993, Technical Editor of the IEEE Transactions on Robotics and Automation from 1989–1994, and Treasurer of the IEEE/ASME Journal of Microelectromechanical Systems from 1992–1997. He was a member of the 1994–1995 National Research Council Committee on Virtual Reality Research and Development. Presently he is Editor of the International Journal of Robotics Research, and Vice President Elect for Conference Activities of the IEEE Robotics and Automation Society. His research interests combine robotics, virtual reality, and human motor control.

Martin Buehler (S'85–M'90) received the Ph.D. degree in electrical engineering from Yale University, New Haven, CT, in 1990.

He was a Postdoctoral Fellow at LegLab, Massachusetts Institute of Technology (MIT). In 1991, he joined McGill University, Montreal, QC, Canada, as the Natural Sciences and Engineering Research Council (NSERC) Junior Industrial Research Chair and a Scholar of the Canadian Institute for Advanced Research. He founded and headed the Ambulatory Robotics Laboratory. In 2003, he joined Boston Dynamics, Cambridge, MA, where he is currently the Director of Robotics. He is currently on the Editorial Board of the *International Journal of Robotics Research* and the *Journal of Field Robotics*. He is the author or coauthor of more than 100 published papers on robotics, and has supervised over 30 graduate students at McGill University.

Dr. Buehler received McGill's William Dawson Scholar Award in 2003. From 1998 to 2003, he was an Associate Editor of the IEEE TRANSACTIONS ON ROBOTICS AND AUTOMATION.